ORIGINAL ARTICLE Brain Tumor Res Treat 2026;14(2):91-101 / pISSN 2288-2405 / eISSN 2288-2413
https://doi.org/10.14791/btrt.2025.0047

Check for updates

In Silico Prediction of EZHIP Post-Translational Modification Sites and Small-Molecule High-Throughput Screening for Quantitative EZHIP Modulation

Jimin Moon[1], Jiwon Hwang[1], Chan Chung[1,2]

[1]Department of New Biology, DGIST, Daegu, Korea
[2]New Biology Research Center (NBRC), DGIST, Daegu, Korea

Background Posterior fossa group A (PFA) ependymoma is a lethal pediatric brain tumor driven predominantly by epigenetic dysregulation. Enhancer of Zeste Homologs Inhibitory Protein (EZHIP) is a defining oncogenic factor in PFA ependymoma that inhibits PRC2 activity, inducing a global loss of H3K27me3 and sustaining aberrant developmental transcriptional programs. Although the metabolic modulator, metformin, reduces EZHIP protein levels, the mechanisms governing EZHIP regulation remain undefined.

Methods We generated a stable HEK293T reporter cell expressing HA- and RFP-tagged EZHIP together with a GFP viability control, enabling quantitative and viability-normalized assessment of EZHIP abundance. *In silico* post-translational modification prediction was performed using PhosphoSitePlus and NetPhos 3.1 to identify candidate regulatory residues and upstream kinases. A focused panel of pathway targeting compounds was evaluated using fluorescence-based high-throughput screening, followed by secondary validation including cell counting, LC_{50} (half-maximal lethal concentration) analysis, and Western blotting.

Results Computational analyses identified multiple high-confidence serine phosphorylation sites on EZHIP and implicated AMPK, MAPK, PKC, AKT, and CK2 signaling pathways. High-throughput screening revealed that activation of the AMPK axis robustly suppressed EZHIP protein levels. Secondary validation demonstrated that biguanides activating AMPK reduced EZHIP abundance independently of cytotoxicity and restored global H3K27me3 levels. In contrast, PKC activation increased EZHIP protein abundance.

Conclusion Our study identifies EZHIP as a dynamically regulated oncoprotein controlled by post-translational signaling pathways. AMPK and PKC exert opposing effects on EZHIP stability, defining actionable regulatory mechanisms for therapeutic targeting in EZHIP-driven cancers.

Keywords EZHIP protein; Ependymoma; Post-translational modification; High-throughput screening assay; Drug development.

Received December 31, 2025
Revised February 10, 2026
Accepted March 1, 2026

Correspondence
Chan Chung
Department of New Biology, DGIST, 333 Techno Jungang-daero, Hyeonpung-myeon, Dalseong-gun, Daegu 42988, Korea
Tel: +82-53-785-1660
Fax: +82-53-785-1819
E-mail: chungc@dgist.ac.kr

INTRODUCTION

Posterior fossa ependymomas represent one of the most common malignant brain tumors in infants and young children [1]. Among them, posterior fossa group A (PFA) ependymoma has emerged as a clinically and molecularly distinct subtype predominantly driven by non-genetic mechanisms [2]. PFA tumors arise mainly during early childhood, recur frequently despite maximal safe surgical resection followed by focal radiotherapy, and exhibit markedly lower long-term survival than other ependymoma subgroups [3]. Although advances in neurosurgery, radiation planning, and supportive care have extended patient lifespan, tumor relapse and treat-

ment resistance remain the defining clinical challenges [4]. The absence of recurrent coding mutations highlights a fundamental epigenomic dependency, positioning chromatin-based vulnerabilities as central drivers of disease biology and making them primarily tractable through regulatory modulation.

Enhancer of Zeste Homologs Inhibitory Protein (EZHIP), also known as CXorf67, is the defining molecular driver of PFA ependymoma [5]. High EZHIP expression is observed in the majority of PFA tumors, whereas other ependymoma subtypes typically show minimal or absent expression [6]. EZHIP directly binds EZH2, the catalytic subunit of the polycomb repressive complex 2 (PRC2), inhibits H3K27 methyltransferase activity, and induces global H3K27me3 depletion [7]. This chromatin state phenocopies the epigenetic mechanism described in H3K27M-mutant diffuse midline gliomas, despite PFA tumors rarely harboring canonical histone mutations [8]. Diminished H3K27me3 disrupts PRC2-mediated transcriptional insulation and lineage-restrictive programs. This permissive chromatin environment supports oncogenic transcriptional modules associated with stemness and mitogenic signaling, while also impairing neural identity maintenance [6, 9-11].

EZHIP-driven epigenetic dysregulation extends beyond tumors in the posterior fossa. A subset of osteosarcomas, an aggressive bone malignancy characterized by pronounced chromosomal rearrangements but scarce recurrent driver mutations, exhibits aberrant EZHIP expression in approximately 20% of patient cohorts across independent datasets [12]. In EZHIP-positive osteosarcoma, high EZHIP abundance correlates with poor response to neoadjuvant therapy, decreased overall survival probability, PRC2 inhibition, global H3K27me3 depletion, developmental gene reactivation, and impaired mesenchymal progenitor differentiation. Loss-of-function modeling demonstrates that reducing EZHIP restores residual H3K27me3, restricts developmental gene activation, decreases proliferation, and disrupts tumor-supporting epigenomic plasticity and aberrant lineage commitment toward smooth muscle fate [12]. These findings reinforce that EZHIP protein stability, rather than genetic alteration, constitutes a therapeutically relevant and potentially druggable vulnerability suitable for small-molecule regulatory screening.

Metformin, a widely used biguanide compound, has recently been explored for its metabolic effects in EZHIP-expressing tumors [13]. Initially applied to reduce tumor-associated metabolites elevated by EZHIP activity, metformin has been observed in preclinical models to additionally reduce EZHIP protein levels while suppressing tumor growth in PFA ependymoma [13]. Although this dual reduction effect is reproducible, the molecular basis underlying metformin-associated EZHIP suppression remains undefined. Current evidence confirms the phenomenon, yet it does not identify the signaling cascade or post-translational modification (PTM)-dependent regulatory mechanisms responsible for the decline of the EZHIP protein abundance.

In this study, we established HEK293T cells engineered to express EZHIP and performed a comprehensive computational prediction of EZHIP PTM sites using publicly accessible *in silico* platforms. Small molecules predicted to influence these PTMs were screened through high-throughput platforms to quantify EZHIP protein modulation and assess EZHIP-dependent survival dynamics in cell-based models.

MATERIALS AND METHODS

Cell culture

HEK293T (ATCC, CRL-3216) cells were cultured in Dulbecco's modified Eagle's medium (DMEM; Welgene, LM001-05) containing 10% fetal bovine serum (Atlas Biologicals, FP-0500-A) and 1% penicillin–streptomycin (Welgene, LS202-02). Cells were grown in the incubator at 37°C with 5% CO_2. All cell lines were routinely tested for mycoplasma contamination.

Stable cell line generation

HEK293T cells were seeded at a density of 7×10^6 cells in 100 mm culture dishes (SPL Life Sciences, 20100). Upon reaching 70%–80% confluence, cells were transiently co-transfected with a plasmid mixture containing pCDH-CMV-TagRFP-EZHIP-HA-EF1α-copGFP-T2A-Puro (2 μg; GenCefe), pMDLg/pRRE (5 μg; Addgene, 12251), pRSV-Rev (5 μg; Addgene, 12253), and pVSV-G (3.2 μg; Addgene, 138479). The plasmids were diluted in serum-free DMEM and combined with 40 μg GeneFect transfection reagent (TransLab, TLC-001). After incubation for 30 min at room temperature, the transfection complexes were added dropwise to the cells. The viral supernatant was harvested 48 hrs post-transfection, clarified by centrifugation at 3,000 rpm for 4 min at 4°C, and filtered using a 0.45 μm syringe filter (Cytiva, 4614). For transduction, recipient HEK293T cells were seeded at 2.4×10^6 cells per 100 mm dish and incubated with the filtered viral stock for 48 hrs. Transduced cells were selected with puromycin (3 μg/mL; BIOMAX, SMP025) for at least 5 passages to establish a stable cell line.

Drug concentration

The working concentrations were determined based on published studies, cited as references, reporting target protein inhibition or activation at concentrations below LC_{50} (half-maximal lethal concentration). The working concentrations, product numbers, and corresponding references for all drugs used are listed below:

BAY 11-7082 (MedChemExpress, MCE, HY-13453); 2 μM

[14], Metformin (Tokyo Chemical Industry, TCI, M2009); 5 mM [15], Phenformin (MCE, HY-16397A); 50 μM [16], Buformin (MCE, HY-B2099A); 50 μM [17], A-769662 (MCE, HY-50662); 5 μM [18], MK-8722 (MCE, HY-111363); 100 nM [19], AICAR (MCE, HY-13417); 500 μM [20], SC79 (MCE, HY-18749); 10 μM [21], Recilisib (MCE, HY-101625); 10 μM [22], Ionomycin (MCE, HY-13434); 1 μM [23], A23187 (MCE, HY-N6687); 1 μM [24], Spermine (MCE, HY-B1777); 200 μM [25], Anisomycin (MCE, HY-18982); 5 μM [26], Forskolin (MCE, HY-15371); 10 μM [27], Phorbol 12-myristate 13-acetate, PMA (MCE, HY-18739); 50 nM [28], Dexamethasone (MCE, HY-14648); 1 μM [29], LY294002 (MCE, HY-10108); 10 μM [30], 3-Methyl Adenine (MCE, HY-19312); 5 mM [31], Decitabine (MCE, HY-A0004); 1 μM [32], Azacitidine (MCE, HY-10586); 1 μM [33], Bobcat339 (MCE, HY-111558A); 5 μM [34], JQ1 (MCE, HY-13030); 10 μM [35], C646 (MCE, HY-13823); 10 μM [36], GSK-J4 (Cayman Chemical, 12073); 1 μM [37], Tazemetostat (MCE, HY-13803); 10 μM [38], GSK126 (MCE, HY-13470); 10 μM [39].

Histone extraction

Cells were harvested and lysed in a hypotonic buffer consisting of 10 mM Tris–HCl (pH 8.0; Biostem, M1364), 1 mM KCl (Sigma, P3911), and 1.5 mM $MgCl_2$ (Sigma, M9272), supplemented with a protease inhibitor cocktail (Roche, 11873580001) and phosphatase inhibitors (Apexbio, K1015). Nuclei were pelleted by centrifugation at 10,000×g for 10 min at 4°C. Histones were extracted by resuspending the nuclear pellet in 0.4 N H_2SO_4 (Sigma, 258105) and rotating overnight at 4°C. After centrifugation to remove debris, the supernatants were precipitated with trichloroacetic acid (TCA; Sigma, T4885) to a final concentration of approximately 25% on ice for 30 min. The histone pellets were collected by centrifugation at 16,000×g for 10 min at 4°C, washed twice with ice-cold acetone (Duksan, D507), and air-dried at room temperature. Pellets were resuspended in autoclaved distilled water.

Western blot assay

For whole cell lysate (WCL), cells were lysed on ice with RIPA buffer (Biomax, BRA0500) supplemented with a protease inhibitor cocktail and phosphatase inhibitors. Samples were sonicated and centrifuged at 15,000 rpm for 15 min at 4°C. Protein concentrations of WCL and histone samples were determined using a BCA assay (Biomax, BCA0500). For Western blot analysis, proteins (10 μg WCL or 1 μg histone) were mixed with 5× SDS-PAGE sample buffer (TransLab, TLP-102.1) and resolved by SDS-PAGE using Ez-PAGE Gel Solution (TransLab; TLP-S05 for 5% stacking gels; TLP-R08 for 8% resolving gels, or TLP-R12 for 12% resolving gels). WCL samples were resolved on 8% resolving gels, and histone samples on 12% resolving gels. Electrophoresis was conducted using ProNA G-Effect (TransLab, TLP-105). Proteins were transferred to PVDF membranes (Merck, IPVH00010) using the Trans-Blot Turbo Transfer System (Bio-Rad). Briefly, membranes were blocked with 5% skim milk (MBcell, MB-S1667) in TBS-T (Biostem, M1310) for 1 hr at room temperature and then incubated with primary antibodies against HA (1:20,000; BioLegend, 901501), VINCULIN (1:20,000; Sigma, V9264), β-actin (1:10,000; Bioss, bsm-33036M), H3K27me3 (1:5,000; Abclonal, A16199), or total H3 (1:5,000; Cell Signaling, 3638S) overnight at 4°C. Following three washes with TBS-T, the membranes were incubated with secondary antibodies against mouse (1:10,000; Bio-Rad, 170-6516) or rabbit (1:10,000; Bio-Rad, 170-6515) for 2 hrs at room temperature. Immunoreactive bands were visualized using WestGlow PICO PLUS ECL reagents (Biomax, BWP0400) and the Fusion FX imaging system (Vilber). Band intensities were quantified using EvolutionCapt Edge software.

High-throughput screening (HTS)

HEK293T-EZHIP cells were seeded in clear-bottom, black 96-well plates (SPL Life Sciences, 33396) at a density of 3×10^3 cells/well. Following incubation for 24 hrs, cells were treated with compounds for 48 hrs. Fluorescence intensities were measured using a BioTek Synergy HTX Multimode Reader (BioTek Instruments, BTS1LASI) in bottom-read mode. Green fluorescent protein (GFP; Ex/Em 485/528 nm) signals were used to estimate cell viability, while red fluorescent protein (RFP; Ex/Em 530/590 nm) signals indicated EZHIP expression levels. Normalized EZHIP levels were calculated using the following formula: [(Compound RFP intensity)/(Compound GFP intensity)]/[(Control RFP intensity)/(Control GFP intensity)]×100%. Each condition was measured in technical triplicate in at least three independent experiments.

Cell counting

Cells were seeded in 96-well plates (3×10^3 cells/well) and incubated for 24 hrs. Cells were then treated with 50nM PMA, 5uM anisomycin, or 10uM recilisib for 48 hrs, detached with Trypsin-EDTA (Welgene, LS015-10), neutralized with complete medium, and centrifuged (3,000 rpm, 4 min, room temperature). Pellets were resuspended in 500 μL medium, mixed 1:1 with 0.4% Trypan Blue, and viable cells were counted using an EVE™ Plus automated cell counter (Nanoentek) by averaging four fields per sample.

Cell viability assay

Cells were seeded into 96-well plates (3×10^3 cells/well) in 100 μL of growth medium and incubated for 24 hrs. Cells were then treated with phenformin or buformin at the concentra-

tions indicated (0–2,500 μM) in fresh medium for 48 hrs. Following treatment, Cell Counting Kit-8 (CCK-8; Dojindo, CK04-13) reagent (10 μL; 1:10) was added to each well, and plates were incubated for 1 hr at 37°C protected from light. After shaking for 1 min and removing bubbles, absorbance at 450 nm was measured using a BioTek Synergy HTX multi-mode reader (BioTek Instruments).

Statistical analysis

Data visualization and statistical analyses were performed using GraphPad Prism (version 10.4.1; GraphPad Software). Comparisons between two groups were performed using unpaired two-tailed t-tests. Statistical analysis for cell counting experiment was performed using two-way anlaysis of variance (ANOVA), followed by Šídák's multiple comparisons test to compare column means. Cell viability was normalized to the 0 μM control, and LC_{50} values were determined by nonlinear regression (log(inhibitor) vs. response, three parameters). For the drug-screening experiments involving multiple compounds compared with control, ordinary one-way ANOVA followed by Dunnett's multiple comparisons test (compound vs. control) was used. A p-value <0.05 was considered statistically significant. The statistical tests used for each experiment are indicated in the figure legends.

RESULTS

Establishment of a stable EZHIP-expressing cell line

To enable small-molecule screening, we generated an EZHIP-expressing stable cell line using a lentiviral construct based on the pCDH-CMV vector (Fig. 1A). The plasmid encodes human EZHIP fused to both HA and RFP tags. The RFP fusion enabled quantitative monitoring of EZHIP abundance through fluorescence intensity, while the HA tag allowed for a clear distinction between endogenous and exogenous EZHIP. In addition, GFP driven by a separate EF-1α promoter was incorporated to serve as a reporter for cell number and as an internal normalization control. The lentiviral construct was transduced into HEK293T cells, and stable integration was confirmed by Western blot analysis using an HA antibody. EZHIP-expressing cells displayed a reduction in global H3K27me3 levels, recapitulating a hallmark epigenetic feature of PFA ependymoma (Fig. 1B). To assess subcellular localization, cells were imaged by fluorescence microscopy. RFP-tagged EZHIP localized predominantly to the nucleus, whereas GFP was distributed throughout the cytoplasm (Fig. 1C).

Identification of potential regulators of EZHIP

To investigate whether EZHIP is regulated through PTMs,

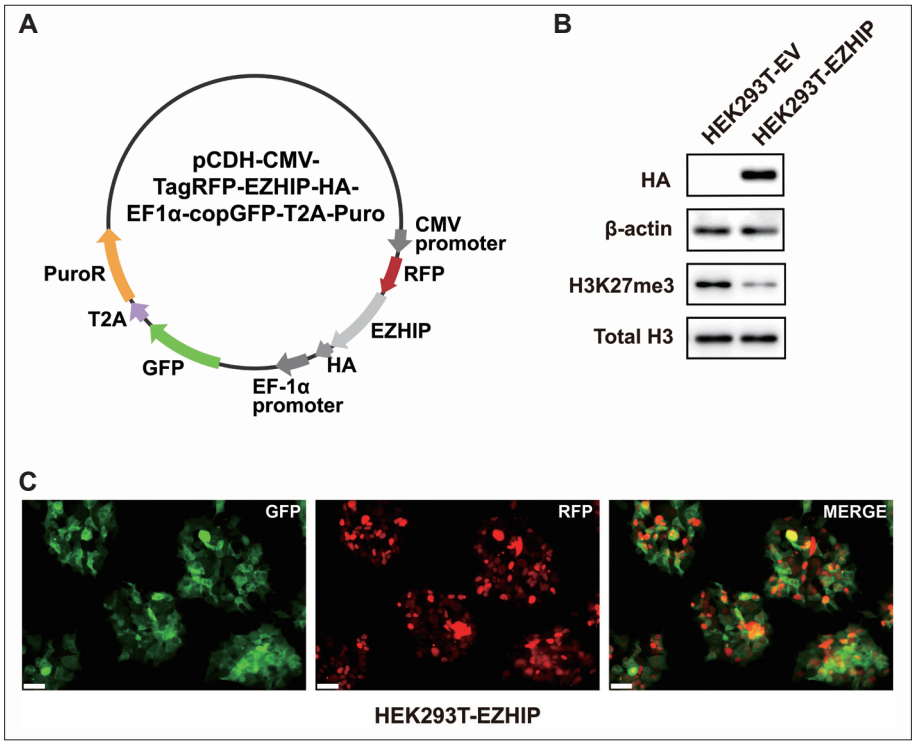

Fig. 1. Global reduction of H3K27me3 following EZHIP overexpression in HEK293T-EZHIP cells. A: Schematic map of the pCDH-CMV-TagRFP-EZHIP-HA-EF1α-copGFP-T2A-Puro lentiviral vector used to generate HEK293T-EZHIP stable line. B: Western blot analysis of HA-tagged EZHIP and H3K27me3 levels in HEK293T-empty vector (EV) and HEK293T-EZHIP. β-actin and total H3 served as loading controls. C: Representative fluorescence images showing GFP and RFP expression in HEK293T-EZHIP cells (Scale bars, 50 μm). GFP, green fluorescent protein; RFP, red fluorescent protein.

A

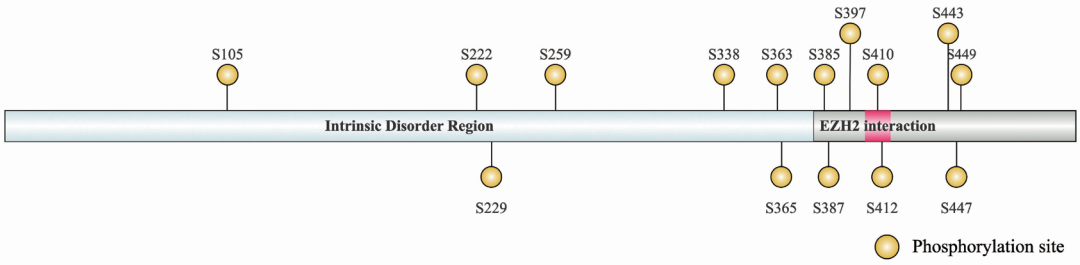

B

Position (aa)	Residue (aa)	Sequence	Predicted kinases
105	S	QDCR S PHEV	CaMK / CK2 / PKA / PKC /
222	S	TLVA S ALRR	CDK / CK2 / MAPK
229	S	RRRA S GPGP	CDK / CK2 / MAPK
259	S	PARL S PESA	AKT / CK2 / PKA / PKC
338	S	HRST S TTPG	CDK / MAPK / PKC
363	S	RRSL S GSAD	CDK / MAPK / RSK
365	S	SLSG S ADEN	CDK / MAPK / RSK
385	S	FQSR S GSPD	CDK / CK1 / CK2 / MAPK
387	S	SRSG S PDPE	CDK / CK1 / CK2 / MAPK
397	S	PSRA S PPVW	AKT / CK2 / PKC
410	S	MRAS S PSPP	CaMK / CDK / MAPK / PKA
412	S	ASSP S PPGR	CaMK / CDK / MAPK / PKA
443	S	SPSR S PGLS	CK2 / PKA / PKC
447	S	SPGL S PSSP	CK2 / PKA / PKC
449	S	GLSP S SPSP	CK2 / PKA / PKC

Position (aa)	Residue (aa)	Sequence	Predicted kinase
105	S	QDCR S PHEV	MAPK / PKG
222	S	TLVA S ALRR	CDK
229	S	RRRA S GPGP	PKA / RSK
259	S	PARL S PESA	CDK / MAPK
338	S	HRST S TTPG	CDK1 / PKA
363	S	RRSL S GSAD	PKA / RSK
365	S	SLSG S ADEN	CK2
387	S	SRSG S PDPE	CDK5 / GSK3
397	S	PSRA S PPVW	CDK5 / CDK1 / PKA
410	S	MRAS S PSPP	CDK1 / CDK5 / GSK3 / PKB / RSK
412	S	ASSP S PPGR	CDK5 / CK1 / GSK3
443	S	SPSR S PGLS	CDK5 / GSK3 / MAPK
447	S	SPGL S PSSP	CDK5 / CK1 / GSK3
449	S	GLSP S SPSP	CDK1

C

	Pathway	Compound	Working conc.
	Ubiquitination	BAY 11-7082	2 μM
	Metformin-like biguanides	Metformin	5 mM
		Phenformin	50 μM
		Buformin	50 μM
	AMPK activators	A-769662	5 μM
		MK-8722	100 nM
		AICAR	500 μM
Kinase activator	Akt	SC79	10 μM
		Recilisib	10 μM
	CaMKII	Ionomycin	1 μM
	CK2	A23187	1 μM
		Spermine	200 μM
	MAPK (JNK/p38)	Anisomycin	5 μM
	PKA	Forskolin	10 μM
	PKC	PMA	50 nM
	SGK	Dexamethasone	1 μM

	Pathway	Compound	Working conc.
	Autophagy inhibition	LY294002	10 μM
		3-Methyl Adenine	5 mM
Epigenetic inhibitors	DNMT inhibitor	Decitabine	1 μM
		Azacitidine	1 μM
	TET inhibitor	Bobcat339	5 μM
	BET/BRD4 inhibitor	JQ1	10 μM
	p300/CBP inhibitor	C646	10 μM
	KDM6A/B inhibitor	GSK-J4	1 μM
	EZH2 inhibition	Tazemetostat	10 μM
		GSK126	10 μM

Fig. 2. Overview of EZHIP phosphorylation-site predictions and high-throughput screening (HTS) compound selection. A: Schematic of the human EZHIP protein indicating the intrinsically disordered region and the EZH2-interaction domain (magenta). Fifteen putative serine phosphorylation sites are marked (yellow circles). B: Computational prediction of candidate upstream kinases for the 15 serine residues. Motif sequences and predicted kinase candidates are summarized based on PhosphoSitePlus (left) and NetPhos 3.1 (right). C: Compound classification for HTS. Compounds are grouped into kinase pathway modulators (left) and autophagy/epigenetic modulators (right) with their respective working concentrations indicated.

we integrated predictions from three independent PTM analysis platforms: PhosphoSitePlus and NetPhos 3.1. This combined approach identified fifteen serine residues (S105, S222, S229, S259, S338, S363, S365, S385, S387, S397, S410, S412, S443, S447, and S449) as high-confidence phosphorylation candidates (Fig. 2A). Motif analysis using PhosphoSitePlus consistently ranked kinase families such as CK2 (10), CDK (9), MAPK (9), PKA (7), PKC (7), CaMK (3), AKT (2), CK1 (2), and RSK (2) as the most probable upstream regulators of these sites. The numbers in parentheses denote the frequency with which each kinase family was predicted across the analyzed phosphosites (Fig. 2B left). Predictions from NetPhos 3.1 supported these findings and additionally suggested potential involvement of CDK5 (6), GSK3 (5), CDK1 (4), PKA (4), MAPK (3), RSK (3), CDK (2), CK1 (2), PKG (1), CK2 (1), and PKB (1) (Fig. 2B right). Together, these data indicate that serine-rich motifs within EZHIP may be phosphorylated downstream of multiple kinase signaling pathways. To functionally assess these predicted pathways, we assembled a panel of pathway-targeting compounds (Fig. 2C). To further evaluate the effect of metformin and its potential dependence on AMPK signaling, we included metformin analogs (phenformin hydrochloride and buformin hydrochloride) as well as diverse AMPK activators (A-769662, MK-8722, and AICAR). Given that EZHIP alters histone modification patterns, we also included a set of epigenetic inhibitors to test whether chromatin-modifying enzymes contribute to EZHIP regulation. Finally, to test the potential role of ubiquitin-mediated degradation, we inhibited ubiquitination using BAY 11-7082 (Fig. 2C).

Fluorescence-based HTS of EZHIP regulators

A stable HEK293T–EZHIP reporter line was seeded into 96-well plates and treated with the small molecule panel shown in Fig. 2C. In this system, GFP fluorescence reflected viable cell number (Fig. 3A), whereas RFP intensity reported EZHIP abundance. EZHIP levels were quantified by normalizing RFP to GFP, thereby restricting analysis to live cells and decoupling EZHIP changes from cell proliferation (Fig. 3B-D). Heatmap analysis of GFP intensity revealed heterogeneous effects on cell viability across the compound panel. AICAR, spermine, PMA, and tazemetostat maintained GFP levels similar to the vehicle control, indicating minimal cytotoxicity (Fig. 3A). In contrast, anisomycin induced the strongest decrease in GFP signal. Metformin-like biguanides (phenformin and buformin) also produced substantial reductions in GFP intensity. Additionally, the DNMT inhibitors (decitabine and azacitidine) as well as the KDM6A/B inhibitor (GSK-J4) markedly suppressed GFP fluorescence (Fig. 3A). These findings indicate that whereas certain compounds substantially reduce cell viability, others have no discernible effect on cell viability.

Normalized RFP/GFP measurements revealed distinct effects on EZHIP regulation (Fig. 3B-D). Consistent with previous observations [13], metformin decreased EZHIP abundance. Additional suppressors included phenformin, buformin, MK-8722, recilisib, forskolin, LY294002, GSK-J4, and GSK126, with A-769662 and AICAR producing the most substantial decreases in the heatmap. In contrast, PMA robustly increased EZHIP levels, representing one of the most substantial upregulating effects in the screen. Although anisomycin showed an apparent increase in normalized EZHIP signal, this effect coincided with a marked reduction in GFP intensity, suggesting that the elevated RFP/GFP ratio may primarily reflect severe loss of cell viability rather than a direct upregulation of EZHIP. Among DNMT inhibitors, azacitidine increased EZHIP as previously reported [40], whereas decitabine had minimal impact. Several compounds, including SC79, dexamethasone, JQ1, tazemetostat, ionomycin, A23187, spermine, 3-methyl adenine, bobcat339, and C646, did not statistically alter EZHIP levels compared to the control (Fig. 3B-D). Because EZHIP quantification was normalized to GFP, these changes reflect specific regulatory effects rather than secondary consequences of altered viability. Together, these data demonstrate that activation of the AMPK axis suppresses EZHIP levels, whereas PKC activation and DNA hypomethylation drive robust EZHIP upregulation, revealing multiple candidate pathways involved in EZHIP regulation.

Secondary validation of HTS hits confirms viability-independent regulation of EZHIP and H3K27me3

To validate the fluorescence-based screening results shown in Fig. 3, we performed a series of secondary assays designed to independently assess cell viability, EZHIP protein regulation, and downstream chromatin effects. First, to confirm that GFP fluorescence accurately reflected cell viability in the screening platform, representative compounds that produced substantial viability changes in the HTS were selected for direct cell counting analysis. Consistent with the GFP-based readouts, anisomycin treatment led to a pronounced reduction in cell number, whereas recilisib treatment increased cell number. In contrast, PMA, which showed minimal effects on GFP signal, did not substantially alter cell viability (Fig. 4A). It validates GFP as a reliable surrogate for cell survival in the HTS assay. Next, compounds that showed increased EZHIP signal in the screening data were further examined by Western blotting to determine whether these effects reflected actual changes in EZHIP protein abundance. Treatment with PMA, a strong EZHIP upregulator identified in the screen, resulted in a robust increase in HA-tagged EZHIP protein levels (Fig. 4B), confirming that the screening signal corresponded to genuine EZHIP protein induction rather than fluorescence arti-

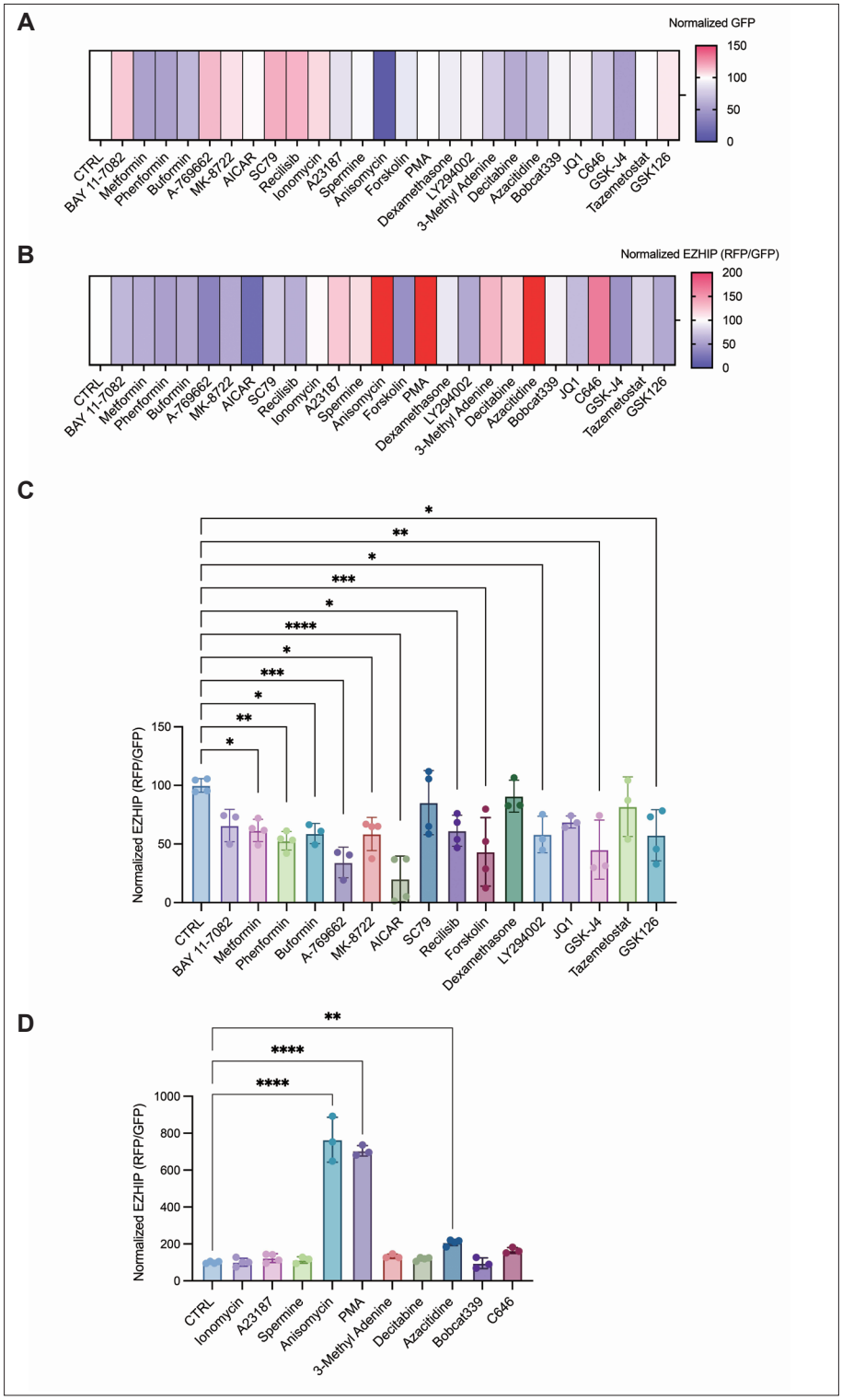

Fig. 3. Fluorescence-based identification of compounds that decrease or increase EZHIP abundance. A: Heatmap of cell viability, expressed as a percentage of vehicle control (CTRL), estimated from GFP fluorescence following treatment with the indicated compounds. Normalized GFP levels were calculated as [(Compound GFP intensity)/(CTRL GFP intensity)]×100%. B: Heatmap of normalized EZHIP levels for the same treatments, calculated from the RFP-to-GFP ratio (RFP/GFP) and expressed relative to CTRL. Normalized EZHIP (%) was calculated as [(Compound RFP intensity)/(Compound GFP intensity)]/[(CTRL RFP intensity)/(CTRL GFP intensity)]×100%. C and D: Quantification of normalized EZHIP levels for selected ubiquitin-pathway, kinase-pathway, autophagy, and epigenetic modulators. Compounds that decrease normalized EZHIP are shown in panel C, whereas compounds that increase normalized EZHIP are shown in panel D. Statistical significance was assessed by ordinary one-way ANOVA followed by Dunnett's multiple-comparisons test (compound vs. CTRL). Significance: *p<0.05; **p<0.01; ***p<0.001; ****p<0.0001.

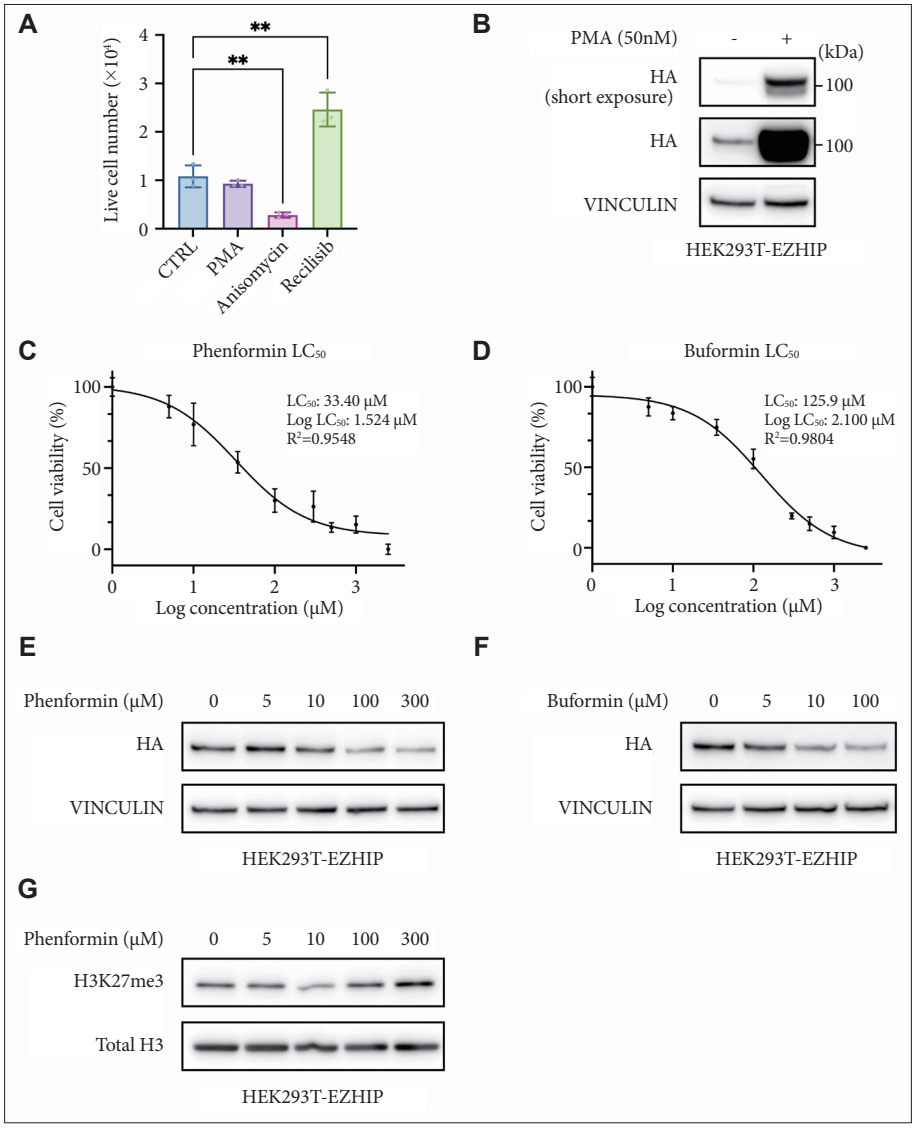

Fig. 4. Regulation of EZHIP protein levels by PKC signaling and biguanide treatment. A: Live cell numbers of HEK293T-EZHIP cells following treatment with the indicated compounds (PMA, anisomycin, or recilisib). Statistical significance was assessed by two-way ANOVA with multiple-comparisons test (compound vs. CTRL). Significance: $^{**}p<0.01$. B: Western blot analysis of HA-tagged EZHIP in HEK293T-EZHIP cells treated with PMA (50 nM) or vehicle control. Vinculin serves as a loading control. C and D: Dose-response curves for cell viability following phenformin (C) or buformin (D) treatment. Viability was normalized to vehicle control and plotted against log-transformed drug concentration. LC_{50} values: phenformin LC_{50}=33.40 μM; buformin LC_{50}=125.9 μM. E and F: Western blot analysis of EZHIP-HA in HEK293T-EZHIP cells with dose dependent treatment of phenformin (E; 0–300 μM) or buformin (F; 0–100 μM). G: Western blot analysis of global H3K27me3 levels in HEK293T-EZHIP cells with dose-dependent treatment of phenformin (0–300 μM). Total H3 is shown as a loading control.

facts. To determine whether EZHIP modulation observed in the screen could be attributed to nonspecific cytotoxic effects, we next assessed the LC_{50} of biguanide compounds. The LC_{50} values were determined to be 33.40 μM for phenformin and 125.9 μM for buformin (Fig. 4C and D). To compare LC_{50} values with the extent of EZHIP protein reduction, phenformin and buformin were administered across a range of concentrations, and EZHIP protein levels were assessed by Western blotting (Fig. 4E and F). Both compounds exhibited a clear concentration-dependent decrease in EZHIP abundance. Importantly, EZHIP suppression was observed at concentrations that did not induce overt cytotoxicity, indicating the presence of a non-lethal concentration window in which phenformin and buformin effectively reduce EZHIP expression. Furthermore, treatment with increasing concentrations of phenformin resulted in a concomitant increase in global H3K27me3 levels that closely paralleled the reduction in EZHIP protein, while total histone H3 levels remained unchanged (Fig. 4G).

Together, these experiments validate the HTS findings by demonstrating that the observed EZHIP modulation is not a secondary consequence of cytotoxicity, but instead reflects a specific regulatory effect. Moreover, biguanide-mediated EZHIP

suppression functionally restores global H3K27me3 levels, supporting a direct link between EZHIP abundance and PRC2-dependent chromatin regulation.

DISCUSSION

EZHIP has been identified in PFA ependymoma since its discovery in 2018 [5,7,40,41]. It is highly expressed in PFA ependymoma and H3-wildtype diffuse midline glioma [42], and has also been reported in subsets of pediatric medulloblastoma, high-grade glioma [43], endometrial stromal sarcoma [44], squamous non-small cell lung cancer [45], and osteosarcoma [12]. EZHIP functions as an intrinsic inhibitor of the PRC2, leading to a global reduction in H3K27me3 and reactivation of developmental and neuronal gene programs, thereby acting as an oncogenic driver across multiple tumor contexts [6,7,43]. In particular, EZHIP has been shown to profoundly reprogram cellular metabolism in PFA ependymoma [13]. Notably, similar metabolic alterations have also been observed in H3K27M-altered diffuse midline gliomas, which share closely related epigenetic features with EZHIP-expressing tumors [46,47]. Beyond metabolic reprogramming, EZHIP reshapes three-dimensional genome organization and establishes aberrant transcriptional networks in PFA ependymoma, further reinforcing malignant phenotypes [48]. More recently, EZHIP has also been implicated in impairing homologous recombination–mediated DNA repair by disrupting key repair protein interactions, thereby promoting genomic instability and creating potential therapeutic vulnerabilities, including sensitivity to PARP inhibition [49]. Collectively, these findings have motivated efforts to identify therapeutic strategies that aim to reduce EZHIP expression or function in cancer.

To systematically interrogate regulators of EZHIP protein abundance, we established an HTS platform capable of quantitatively measuring EZHIP protein levels via RFP fluorescence intensity. To control for cell viability and transcriptional effects, a separate GFP reporter was incorporated into the EZHIP expression construct as an internal reference. Using three independent PTM prediction algorithms, we identified candidate regulatory pathways potentially governing EZHIP abundance. Based on these predictions, small molecules targeting the inferred modification pathways were selected and evaluated using the HTS system. Consistent with prior studies, AMPK activation was found to be a robust mechanism for EZHIP suppression. Previous work demonstrated that metformin, an AMPK activator that inhibits mitochondrial complex I and increases the AMP/ATP ratio, reduces EZHIP protein abundance while restoring global H3K27me3 levels in EZHIP-expressing PFA cells [13]. Similar effects were observed with the AMPK activator AICAR, supporting an AMPK-dependent regulatory mechanism [13]. Our HTS results are in strong agreement with these findings. Notably, all AMPK activators, such as phenformin and buformin, reduced EZHIP levels in our study, with AICAR producing the most pronounced effect. Furthermore, phenformin and buformin were selected for secondary validation because they simultaneously reduced cell viability and EZHIP protein levels. Both compounds also led to increased H3K27me3, reinforcing the functional link between EZHIP suppression and epigenetic restoration.

In contrast, treatment with the PKC activator PMA unexpectedly increased EZHIP protein abundance to approximately 700% of control levels. This observation suggests that kinase signaling can exert divergent and context-dependent effects on EZHIP regulation. To date, no studies have directly examined kinase-mediated control of EZHIP, making it difficult to infer how activation of PKC pathways leads to increased EZHIP protein stability or accumulation. These findings highlight a critical gap in our understanding of EZHIP post-translational regulation and underscore the need for additional mechanistic studies.

Together, our study establishes EZHIP as a dynamically regulated oncoprotein whose abundance is controlled by multiple post-translational signaling pathways. While AMPK activation consistently suppresses EZHIP and restores repressive chromatin states, activation of PKC signaling unexpectedly increases EZHIP protein levels, revealing unanticipated regulatory complexity. These findings expand current understanding of EZHIP regulation and suggest that context-dependent kinase signaling may critically influence EZHIP-driven tumor phenotypes. Elucidating the molecular mechanisms through which AMPK and PKC regulate EZHIP will be essential for refining therapeutic strategies targeting EZHIP-dependent cancers.

Ethics Statement

This study did not involve human participants or human-derived clinical specimens, nor did it include animal experiments. All experiments were performed using established and commercially available cell lines. Therefore, ethical approval and informed consent were not required for this study.

Availability of Data and Material

All data generated or analyzed during the study are included in this published article.

ORCID iDs

Jimin Moon https://orcid.org/0009-0005-2534-4410
Jiwon Hwang https://orcid.org/0009-0000-3879-4828
Chan Chung https://orcid.org/0000-0003-0510-8996

Author Contributions

Conceptualization: Chan Chung. Data curation: Jimin Moon, Jiwon Hwang. Formal analysis: Jimin Moon, Jiwon Hwang. Funding acquisition: Chan Chung. Investigation: Jimin Moon, Jiwon Hwang. Methodology: Ji-

min Moon, Jiwon Hwang. Project administration: Chan Chung. Resources: Chan Chung. Software: Jimin Moon, Jiwon Hwang. Supervision: Chan Chung. Validation: Chan Chung. Visualization: Jimin Moon, Jiwon Hwang. Writing—original draft: Jimin Moon. Writing—review & editing: Chan Chung.

Conflicts of Interest

The authors have no potential conflicts of interest to disclose.

Funding Statement

This work was supported by the Korean Society for Neuro-Oncology (KSNO) Research Funding and the National Research Foundation of Korea (NRF) grant funded by the Ministry of Science and ICT (RS-2022-NR072141).

Acknowledgments

We acknowledge the Korean Society for Neuro-Oncology (KSNO), the Daegu Gyeongbuk Institute of Science and Technology (DGIST), Dr. Sriram Venneti, and the Collaborative Ependymoma Research Network (CERN) Foundation for their leadership in advancing ependymoma research.

REFERENCES

1. Price M, Ballard CAP, Benedetti JR, Kruchko C, Barnholtz-Sloan JS, Ostrom QT. CBTRUS statistical report: primary brain and other central nervous system tumors diagnosed in the United States in 2018-2022. Neuro Oncol 2025;27(Suppl_4):iv1-66.
2. Mack SC, Witt H, Piro RM, Gu L, Zuyderduyn S, Stütz AM, et al. Epigenomic alterations define lethal CIMP-positive ependymomas of infancy. Nature 2014;506:445-50.
3. Pajtler KW, Witt H, Sill M, Jones DT, Hovestadt V, Kratochwil F, et al. Molecular classification of ependymal tumors across all CNS compartments, histopathological grades, and age groups. Cancer Cell 2015;27:728-43.
4. Merchant TE. Current clinical challenges in childhood ependymoma: a focused review. J Clin Oncol 2017;35:2364-9.
5. Pajtler KW, Wen J, Sill M, Lin T, Orisme W, Tang B, et al. Molecular heterogeneity and CXorf67 alterations in posterior fossa group A (PFA) ependymomas. Acta Neuropathol 2018;136:211-26.
6. Jenseit A, Camgöz A, Pfister SM, Kool M. EZHIP: a new piece of the puzzle towards understanding pediatric posterior fossa ependymoma. Acta Neuropathol 2022;143:1-13.
7. Jain SU, Do TJ, Lund PJ, Rashoff AQ, Diehl KL, Cieslik M, et al. PFA ependymoma-associated protein EZHIP inhibits PRC2 activity through a H3 K27M-like mechanism. Nat Commun 2019;10:2146.
8. Jain SU, Rashoff AQ, Krabbenhoft SD, Hoelper D, Do TJ, Gibson TJ, et al. H3 K27M and EZHIP impede H3K27-methylation spreading by inhibiting allosterically stimulated PRC2. Mol Cell 2020;80:726-35.e7.
9. Thornton SR, Butty VL, Levine SS, Boyer LA. Polycomb repressive complex 2 regulates lineage fidelity during embryonic stem cell differentiation. PLoS One 2014;9:e110498.
10. Hamanishi ET, Dang D, Venneti S. Aberrant histone modifications in pediatric brain tumors. Front Oncol 2025;15:1587157.
11. Pun M, Pratt D, Nano PR, Joshi PK, Jiang L, Englinger B, et al. Common molecular features of H3K27M DMGs and PFA ependymomas map to hindbrain developmental pathways. Acta Neuropathol Commun 2023;11:25.
12. Jawhar W, Danieau G, Annett A, Ishii T, Bajic A, Castillo-Orozco A, et al. Aberrant EZHIP expression drives tumorigenesis in osteosarcoma. Nat Commun 2025;16:6752.
13. Panwalkar P, Tamrazi B, Dang D, Chung C, Sweha S, Natarajan SK, et al. Targeting integrated epigenetic and metabolic pathways in lethal childhood PFA ependymomas. Sci Transl Med 2021;13:eabc0497.
14. Strickson S, Campbell DG, Emmerich CH, Knebel A, Plater L, Ritorto MS, et al. The anti-inflammatory drug BAY 11-7082 suppresses the MyD88-dependent signalling network by targeting the ubiquitin system. Biochem J 2013;451:427-37.
15. Xue J, Zhang H, Liu W, Liu M, Shi M, Wen Z, et al. Metformin inhibits growth of eutopic stromal cells from adenomyotic endometrium via AMPK activation and subsequent inhibition of AKT phosphorylation: a possible role in the treatment of adenomyosis. Reproduction 2013;146:397-406.
16. Zhuang D, Wang S, Deng H, Shi Y, Liu C, Leng X, et al. Phenformin activates ER stress to promote autophagic cell death via NIBAN1 and DDIT4 in oral squamous cell carcinoma independent of AMPK. Int J Oral Sci 2024;16:35.
17. Parris AB, Zhao Q, Howard EW, Zhao M, Ma Z, Yang X. Buformin inhibits the stemness of erbB-2-overexpressing breast cancer cells and premalignant mammary tissues of MMTV-erbB-2 transgenic mice. J Exp Clin Cancer Res 2017;36:28.
18. Moreno D, Knecht E, Viollet B, Sanz P. A769662, a novel activator of AMP-activated protein kinase, inhibits non-proteolytic components of the 26S proteasome by an AMPK-independent mechanism. FEBS Lett 2008;582:2650-4.
19. Feng D, Biftu T, Romero FA, Kekec A, Dropinski J, Kassick A, et al. Discovery of MK-8722: a systemic, direct pan-activator of AMP-activated protein kinase. ACS Med Chem Lett 2018;9:39-44.
20. Jose C, Hébert-Chatelain E, Bellance N, Larendra A, Su M, Nouette-Gaulain K, et al. AICAR inhibits cancer cell growth and triggers cell-type distinct effects on OXPHOS biogenesis, oxidative stress and Akt activation. Biochim Biophys Acta 2011;1807:707-18.
21. Jo H, Mondal S, Tan D, Nagata E, Takizawa S, Sharma AK, et al. Small molecule-induced cytosolic activation of protein kinase Akt rescues ischemia-elicited neuronal death. Proc Natl Acad Sci U S A 2012;109:10581-6.
22. Kang AD, Cosenza SC, Bonagura M, Manair M, Reddy MV, Reddy EP. ON01210.Na (Ex-RAD®) mitigates radiation damage through activation of the AKT pathway. PLoS One 2013;8:e58355.
23. Chatila T, Silverman L, Miller R, Geha R. Mechanisms of T cell activation by the calcium ionophore ionomycin. J Immunol 1989;143:1283-9.
24. Cho SY, Lee JH, Bae HD, Jeong EM, Jang GY, Kim CW, et al. Transglutaminase 2 inhibits apoptosis induced by calcium- overload through down-regulation of Bax. Exp Mol Med 2010;42:639-50.
25. Bazin MA, Le Lamer AC, Delcros JG, Rouaud I, Uriac P, Boustie J, et al. Synthesis and cytotoxic activities of usnic acid derivatives. Bioorg Med Chem 2008;16:6860-6.
26. Lu Z, Miao Y, Muhammad I, Tian E, Hu W, Wang J, et al. Colistin-induced autophagy and apoptosis involves the JNK-Bcl2-Bax signaling pathway and JNK-p53-ROS positive feedback loop in PC-12 cells. Chem Biol Interact 2017;277:62-73.
27. Thomas D, Zhang W, Karle CA, Kathöfer S, Schöls W, Kübler W, et al. Deletion of protein kinase A phosphorylation sites in the HERG potassium channel inhibits activation shift by protein kinase A. J Biol Chem 1999;274:27457-62.
28. Hussaini IM, Karns LR, Vinton G, Carpenter JE, Redpath GT, Sando JJ, et al. Phorbol 12-myristate 13-acetate induces protein kinase cetaspecific proliferative response in astrocytic tumor cells. J Biol Chem 2000;275:22348-54.
29. Yu XH, Xu XM, Zhang SX. Low-dose dexamethasone promotes osteoblast viability by activating autophagy via the SGK1/FOXO3a signaling pathway. Cell Biol Int 2023;47:669-78.
30. Blommaart EF, Krause U, Schellens JP, Vreeling-Sindelárová H, Meijer AJ. The phosphatidylinositol 3-kinase inhibitors wortmannin and LY294002 inhibit autophagy in isolated rat hepatocytes. Eur J Biochem 1997;243:240-6.
31. Miller S, Oleksy A, Perisic O, Williams RL. Finding a fitting shoe for Cinderella: searching for an autophagy inhibitor. Autophagy 2010;6:805-7.

32. Buocikova V, Tyciakova S, Pilalis E, Mastrokalou C, Urbanova M, Matuskova M, et al. Decitabine-induced DNA methylation-mediated transcriptomic reprogramming in human breast cancer cell lines; the impact of DCK overexpression. Front Pharmacol 2022;13:991751.
33. Tsujioka T, Yokoi A, Uesugi M, Kishimoto M, Tochigi A, Suemori S, et al. Effects of DNA methyltransferase inhibitors (DNMTIs) on MDS-derived cell lines. Exp Hematol 2013;41:189-97.
34. Chua GNL, Wassarman KL, Sun H, Alp JA, Jarczyk EI, Kuzio NJ, et al. Cytosine-based TET enzyme inhibitors. ACS Med Chem Lett 2019;10:180-5.
35. Zhang Y, Duan S, Jang A, Mao L, Liu X, Huang G. JQ1, a selective inhibitor of BRD4, suppresses retinoblastoma cell growth by inducing cell cycle arrest and apoptosis. Exp Eye Res 2021;202:108304.
36. Yu Z, Taniguchi J, Wei Y, Pandian GN, Hashiya K, Bando T, et al. Antiproliferative and apoptotic activities of sequence-specific histone acetyltransferase inhibitors. Eur J Med Chem 2017;138:320-7.
37. Kruidenier L, Chung CW, Cheng Z, Liddle J, Che K, Joberty G, et al. A selective jumonji H3K27 demethylase inhibitor modulates the proinflammatory macrophage response. Nature 2012;488:404-8.
38. Knutson SK, Warholic NM, Wigle TJ, Klaus CR, Allain CJ, Raimondi A, et al. Durable tumor regression in genetically altered malignant rhabdoid tumors by inhibition of methyltransferase EZH2. Proc Natl Acad Sci U S A 2013;110:7922-7.
39. Woo J, Kim HY, Byun BJ, Chae CH, Lee JY, Ryu SY, et al. Biological evaluation of tanshindiols as EZH2 histone methyltransferase inhibitors. Bioorg Med Chem Lett 2014;24:2486-92.
40. Piunti A, Smith ER, Morgan MAJ, Ugarenko M, Khaltyan N, Helmin KA, et al. CATACOMB: an endogenous inducible gene that antagonizes H3K27 methylation activity of Polycomb repressive complex 2 via an H3K27M-like mechanism. Sci Adv 2019;5:eaax2887.
41. Hübner JM, Müller T, Papageorgiou DN, Mauermann M, Krijgsveld J, Russell RB, et al. EZHIP/CXorf67 mimics K27M mutated oncohistones and functions as an intrinsic inhibitor of PRC2 function in aggressive posterior fossa ependymoma. Neuro Oncol 2019;21:878-89.
42. Antin C, Tauziède-Espariat A, Debily MA, Castel D, Grill J, Pagès M, et al. EZHIP is a specific diagnostic biomarker for posterior fossa ependymomas, group PFA and diffuse midline gliomas H3-WT with EZHIP overexpression. Acta Neuropathol Commun 2020;8:183.
43. Hasheminasabgorji E, Chen HM, Gatesman TA, Younes ST, Nobles GA, Jaryani F, et al. EZHIP boosts neuronal-like synaptic gene programs and depresses polyamine metabolism. Acta Neuropathol Commun 2025;13:227.
44. Dewaele B, Przybyl J, Quattrone A, Finalet Ferreiro J, Vanspauwen V, Geerdens E, et al. Identification of a novel, recurrent MBTD1-CXorf67 fusion in low-grade endometrial stromal sarcoma. Int J Cancer 2014;134:1112-22.
45. Djureinovic D, Hallström BM, Horie M, Mattsson JSM, La Fleur L, Fagerberg L, et al. Profiling cancer testis antigens in non-small-cell lung cancer. JCI Insight 2016;1:e86837.
46. Chung C, Sweha SR, Pratt D, Tamrazi B, Panwalkar P, Banda A, et al. Integrated metabolic and epigenomic reprograming by H3K27M mutations in diffuse intrinsic pontine gliomas. Cancer Cell 2020;38:334-49.e9.
47. Park J, Chung C. Epigenetic and metabolic changes in diffuse intrinsic pontine glioma. Brain Tumor Res Treat 2023;11:86-93.
48. Johnston MJ, Lee JJY, Hu B, Nikolic A, Hasheminasabgorji E, Baguette A, et al. TULIPs decorate the three-dimensional genome of PFA ependymoma. Cell 2024;187:4926-45.e22.
49. Han J, Yu M, Bai Y, Yu J, Jin F, Li C, et al. Elevated CXorf67 expression in PFA ependymomas suppresses DNA repair and sensitizes to PARP inhibitors. Cancer Cell 2020;38:844-56.e7.